Available online at www.sciencedirect.com

SCIENCE DIRECT®

Thin Solid Films 426 (2003) 16–30

thin solid films

www.elsevier.com/locate/tsf

Transmission electron microscopy study of simultaneous high-dose $C^+ + N^+$ co-implantation into (1 1 1)Si

F.M. Morales[a,*], S.I. Molina[a], A. Ponce[a], D. Araújo[a], R. García[a], L. Barbadillo[b], M. Cervera[b], J. Piqueras[b]

[a]*Dpto. de Ciencia de los Materiales e Ingeniería Metalúrgica y Química Inorgánica, Universidad de Cádiz, Apdo. 40, Puerto Real, 11510 Cadiz, Spain*

[b]*Laboratorio de Microelectrónica, Facultad de Ciencias, C-XI 100, Universidad Autónoma de Madrid, 28049 Cantoblanco, Madrid, Spain*

Received 4 February 2002; received in revised form 25 October 2002; accepted 24 November 2002

Abstract

A structural electron microscopy study of (1 1 1)Si samples implanted with $C^+ + N^+$ at low energies (30 keV) and high-doses (5×10^{17} at. cm^{-2} for carbon ions and 6.7×10^{17} at. cm^{-2} for nitrogen ions) is reported in this paper. Implantations were carried out both at room and high (600 °C) temperatures. Samples implanted at high temperature and annealed after implantation show a buried layer consisting of a mixture of some amorphous component and single-crystalline crystallites (SiC and probably Si_3N_4 and C_3N_4) well oriented with respect to the (1 1 1)Si substrate. Both inclusions and amorphous phases are included into a well-aligned Si matrix. The crystalline structure of buried layers resulting after implantation at room and higher temperatures is reviewed. The obtained structural results are confronted to the actual literature. These are encouraging results in order to use the ion implantation to obtain stoichiometric crystalline thin layers.
© 2002 Elsevier Science B.V. All rights reserved.

Keywords: Transmission electron microscopy; Silicon carbide; Silicon nitride; Ion implantation

1. Introduction

Ion implantation has demonstrated to be an ideal method for modifying near-surface properties of materials and offers advantages to accurately control stoichiometry and thickness of surface and buried layers by an appropriate choice of ion energy and dose. This method as a non-equilibrium process is suitable for modulating radiation-induced damage, dopant diffusion, mechanical and electronic properties and for creating new phases and compounds because it allows solid solubility limits to be largely exceeded. Buried layers and interfaces created by implantation of silicon (Si) have fields of application as, for example, in high-efficiency solar cells [1] or in silicon on insulator technologies [2–8].

Silicon carbide (SiC) is a wide band gap semiconductor and has been extensively considered for electronic devices operating at extreme conditions of high temperature (HT), high frequency, high power, high radiation and chemically aggressive ambient. SiC possesses high resistance to oxidation, corrosion, creep and excellent mechanical properties at HTs as a high-strength structural ceramic. Ion beam synthesis allows the formation of SiC at temperatures lower than that used for other standard techniques. The formation of thin SiC surface layers has recently been proposed as suitable substrates for the heteroepitaxial growth of β-SiC on Si [9] or for creating SiC on insulator (SiCOI) structures [8]. SiC buried layers have also been synthesized by carbon ion implantation into silicon and HT annealing by various authors. The bests results (SiC structural quality) were obtained when higher substrate temperatures were used during the implantation process [9–13]. These carbide layers are placed under a thin silicon layer being thus a new viable way to obtain a seed layer for further β-SiC or GaN CVD or MBE growth. Residual stress on the silicon over-layer and the inner presence

*Corresponding author. Tel.: +34-956-016335; fax: +34-956-016288.

E-mail address: fmiguel.morales@uca.es (F.M. Morales).

0040-6090/03/$ - see front matter © 2002 Elsevier Science B.V. All rights reserved.
doi:10.1016/S0040-6090(02)01284-1

of already formed β-SiC well-aligned grains are expected to enhance the essential formation of a thin carbonized layer [14] before SiC or GaN depositions. In this way, other option to facilitate surface carbonizations using implanted Si would be to sacrifice the obtained Si over-layer by oxidation and later removing by etching, thus bringing the SiC buried layer to the surface. On the other hand, applications of semi-insulating SiC buried layers as SOI structures in CMOS devices [6], efficient etch-stop layers suitable for high-quality SWB/SOI substrates (SOI by Si wafer bonding), membranes and micromechanical uses [4,15] or suppression of transient diffusion enhancement (TED) of dopant species [16,17] have been demonstrated for C^+ implanted Si structures.

Silicon nitride (Si_3N_4) is most used in microelectronic industry as an insulator in SOI structures. Some attempts of Separation by IMplanted NItrogen (SIMNI) structures have been successfully carried out by N^+ implantation into silicon [2,3,5]. Nitrogen implantation into Si have been successfully applied for hardening of Si surfaces [18], etch-stop purposes [19,20], partial inhibition of Si oxidation [21], formation of shallow p^+–n junctions in boron doped silicon [22] or stabilisation of SOI buried oxide layers for subsequent epitaxial growth of β-SiC/SOI structures [7]. N^+ implanted Si structures are also used for controlling the thickness in gate oxides [7], applications in gate insulators for metal-oxide semiconductors (MOS) devices [23], buried layers with electric properties [24] and attainment of tribological properties for micromechanic devices [25].

Carbon nitride (C_3N_4) is characterized by high-hardness, high wear resistance and low coefficient of friction. Its chemical, structural, electrical, optical, thermal and mechanical special properties make it an attractive material for industrial operation. There is currently significant experimental [26,27] and theoretical [28,29] interest in the synthesis and properties of C_3N_4 materials due in part to the early prediction that β-C_3N_4 should be as hard as diamond [28]. C_3N_4 phases have been produced by ion beam synthesis using negative carbon and positive nitrogen ions [30], C^+ and N^+ into diamond substrates [31], nitrogen implantation of graphite or glassy carbon [32–34] and N^+ into SiC [35,36], but they were not produced using silicon as a substrate.

Carbon plus nitrogen implantation can be used to obtain compliant substrates. This fact allows a reduction of the lattice constant in the silicon over-layer and the achievement of mechanically flexible surfaces for improving epitaxial overgrowths [37]. The idea of co-implanting carbon and other elements in Si started because carbon can both reduce the lattice strain and facilitate the precipitation in ion beam synthesized IBS/SOI structures [38]. SiC and Si_3N_4 coexistence in implanted Si has been occasionally shown as polycrystalline inclusions [39] but not having well-alignment with respect to the substrate orientation. Other attempts to obtain SiC and Si_3N_4 composites were carried out by implanting N^+ in amorphous SiC [40] or polycrystalline SiC [41].

Table 1
Implantation conditions ((a) Temperature of implantation. (b) Implanted ions doses. (c) Temperature and time of annealing.) for studied samples

Sample	*T* implant	Dose (at. cm^{-2})	*T* annealing/*t*
A	*RT*	6.7×10^{17} N^+	1200 °C/3 h
B	*RT*	6.7×10^{17} N^+ 5×10^{17} C^+	1200 °C/3 h
C	600 °C	6.7×10^{17} N^+ 5×10^{17} C^+	Not
D	600 °C	6.7×10^{17} N^+ 5×10^{17} C^+	1200 °C/3 h

Note that all the implantations were carried out at the same energy of 30 keV.

However, the mechanisms involved in the silicon co-implanted region when two different ions are used become more complex because the mixing of three elements occurs (Si and the two co-implanted elements). The present work studies the structural properties of layers formed by co-implantation of N^+ and C^+ in Si. The structural changes originated in the co-implanted Si region are discussed comparing with literature results obtained by implantation of a unique element (C or N) in Si. The purpose of this work is to understand the material modifications when ion beam synthesis exceeds the solids solubility limits of C and N and to characterize the formation of new phases.

2. Experimental

Both-side polished (1 1 1)Si floating-zone wafers were implanted in a modified Varian Exitron ion implanter. Four samples were implanted at 30 keV using N_2 (in sample A) or a gas mixture of $CO+N_2$ (in the rest of the samples) as ion sources. The implantation doses were 5×10^{17} at. cm^{-2} for carbon ions and 6.7×10^{17} at. cm^{-2} for nitrogen ions. Samples A and B were implanted at room temperature (RT). Sample A was only implanted with N^+ and subsequently annealed at 1200 °C for 3 h. Sample B was implanted with C^+ after the N^+ implantation, and the same post-implantation annealing was applied. The other two specimens (C and D) were $N^+ + C^+$ implanted at HT (600 °C). No annealing was performed in sample C while sample D was annealed at 1200 °C for 3 h. The annealing treatments were made inside a furnace in pure N_2 atmosphere. A schematic view of the implantation conditions is shown in Table 1.

Transmission electron microscopy (TEM), high-resolution electron microscopy (HREM) and selected area

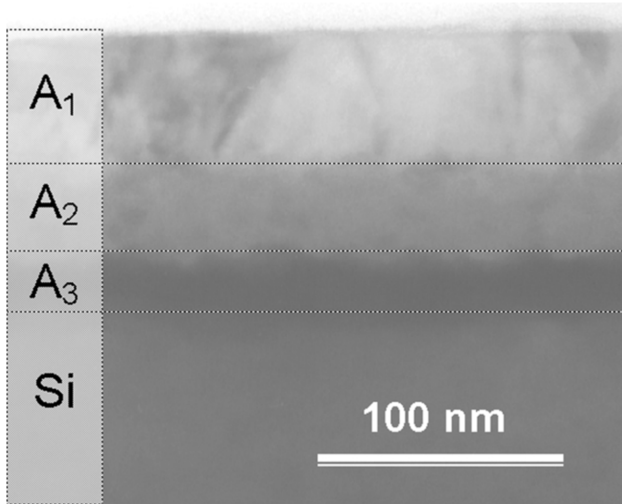

Fig. 1. XTEM image of layered sample A. These layers have an average measured thickness from XTEM images of 50 nm for A_1, 30 nm for A_2 and 20 nm for A_3.

electron diffraction (SAED) were the techniques used to study the inner crystalline structure of the samples. Scanning electron microscopy (SEM) was used to check the samples surface morphology. Specimens were prepared by cross-section TEM (XTEM) and plan view TEM (PVTEM) using mechanical thinning and Ar^+ milling at 4.5 kV in a Gatan Dual Ion Mill system. Conventional TEM was carried out in a JEOL JEM-1200EX electron microscope and a JEOL JEM-2000EX/THR was used for HREM, while SAED analyses were performed in both microscopes. A JEOL 820-JSM was the equipment used for SEM experiments.

3. Results

3.1. Sample A

XTEM images of this sample show three well-defined layers labelled as A_1, A_2 and A_3 in Fig. 1. These layers have an average measured thickness from XTEM images of 50 nm for A_1, 30 nm for A_2 and 20 nm for A_3. SAED patterns were registered from these layers and crystalline Si was detected in the three layers altogether. From these patterns, polycrystalline Si is the unique crystalline phase in layer A_1. Layer A_2 is mostly amorphous and layer A_3 corresponds to twinned single-crystalline Si. In layers A_2 and A_3, Si_3N_4 (α and β) crystalline formations with their (1 1 1) planes misoriented with respect to the (1 1 1) planes of the Si substrate were detected.

Fig. 2 shows a SAED pattern of highly misoriented grains of Si constituting layer A_1 and grains included inside an amorphous matrix in A_2. The polycrystalline/amorphous nature of these layers was confirmed by HREM studies. The SAED pattern of Fig. 3 was registered from layer A_3 near layer A_2. The most intense ordered spots in the pattern are due to the (1 1 1)Si matrix of layer A_3 while the spots situated between the main spots (at distances of 1/3 of the distance between the main spots) are originated by the twinned nature of this deepest region (layer A_3). There are other spots encircled in the pattern of Fig. 3. The one labelled as 'α' corresponds to α-Si_3N_4 for a lattice parameter of 0.208 nm associated to (0 3 1) or (3 3 1) crystalline

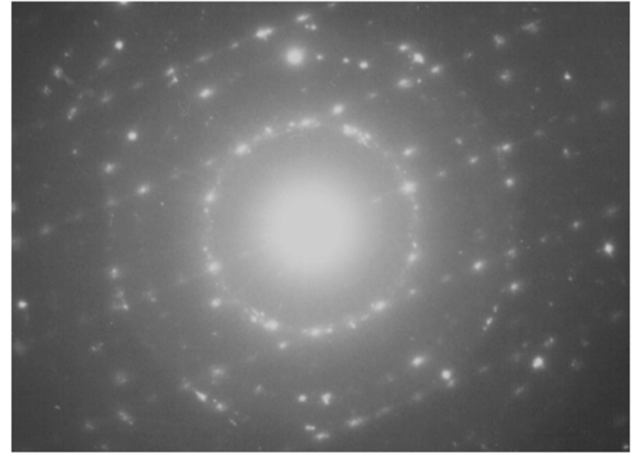

Fig. 2. SAED pattern of layers A_1 and A_2 registered along $[1\,\bar{1}\,0]$. The polycrystalline nature of Si in layer A_1, the amorphous nature of A_2 and the misorientation of grains in both layers are evidenced.

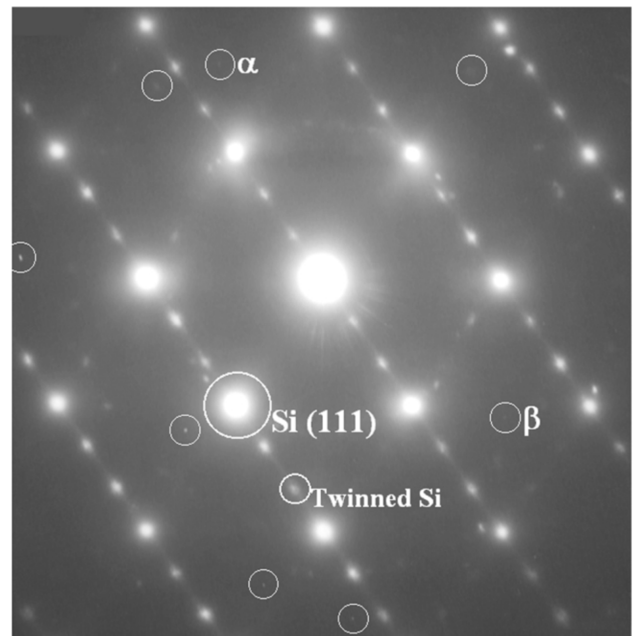

Fig. 3. SAED pattern of layer A_3 near A_2 registered along $[1\,\bar{1}\,0]$. The main ordered spots corresponds to layer A_3 (Si matrix and twins). Spots 'α' and 'β' are due to α- and β-Si_3N_4, respectively, while the rest of the spots encircled are related to α- and/or β-Si_3N_4.

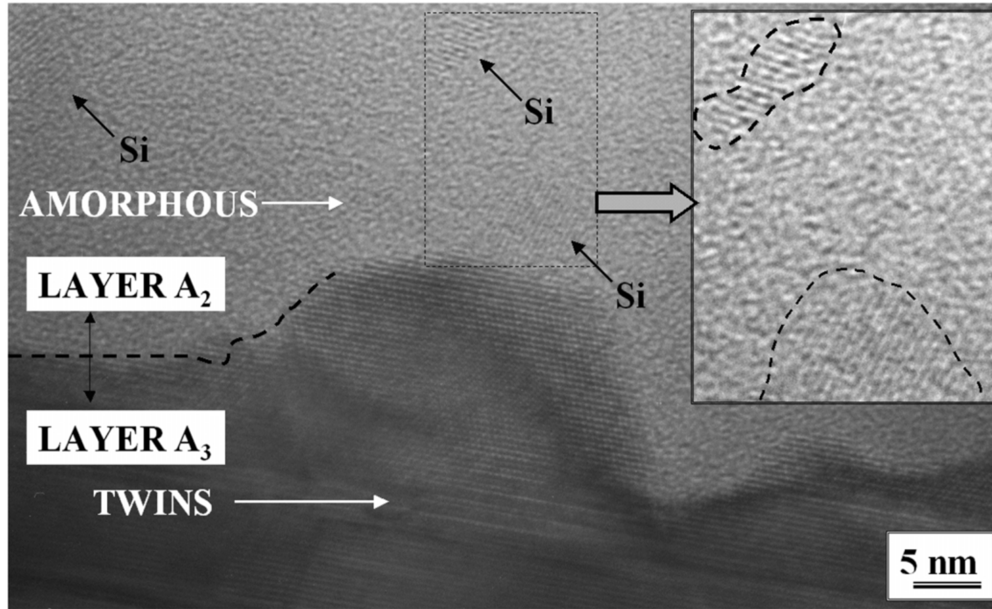

Fig. 4. HREM image of interface A_2/A_3. The inset shows a magnified detail of Si inclusions dispersed into the amorphized layer A_2 while the elongated contrasts inside layer A_3 denotes twin planes.

planes. The diffraction spot labelled as 'β' corresponds to β-Si_3N_4 for a lattice parameter of 0.218 nm, associated to $(0\,2\,1)$ or $(2\,\bar{2}\,1)$ planes of β-Si_3N_4. Spots encircled and without label index for different planes of Si_3N_4 but the distinction between the α and β natures of these polycrystallites was not possible. The rest of the spots in the figure correspond to poly-Si.

HREM images of the A_2/A_3 interface and inside the A_2 amorphous layer were carefully registered in order to detect Si or Si_3N_4 phases and its main characteristics. The infrequent presence of these nitride phases into the amorphous (foreseen by the low intensity of their corresponding diffraction spots) did not allow the observation of nitride isolated grains into the amorphized layer. However, some Si inclusions near the abrupt A_2/A_3 interface were detected as that shown in the HREM image of Fig. 4. These Si inclusions have irregular shapes and are randomly misoriented with respect to the Si matrix. They are generally less than 10 nm in diameter and their areas are smaller than 50 nm^2. Twins are extended along the entire layer A_3. Moreover, X-ray diffraction and FTIR measurements carried out for this sample showed more data, which support the existence of Si–N phases inside this multi-layer structure [39].

3.2. Sample B

XTEM images of this sample show that implantation of N and C at RT and post-annealing originated three well-defined layers (B_1, B_2 and B_3 in Fig. 5a). The HREM and SAED studies revealed that layer B_1 consisted mainly of polycrystalline Si while layer B_2 showed an amorphous structure. Both layers contain inclusions of different crystalline nature inside. SAED patterns of layer B_3 corresponds to single-crystalline Si, but bright field XTEM images of this layer showed a darker contrast than layers B_1 and B_2, probably associated to the presence of N and C atoms solved in the Si matrix without having changed the Si single-crystalline structure. Average thicknesses measured from XTEM images are 82 nm for layer B_1, 85 nm for layer B_2 and 22 nm for layer B_3. More detailed study of this sample can be found in an earlier publication [39].

Fig. 5b shows a typical SAED pattern belonging to the three layers of sample B. In this pattern, the main ordered spots are due to the diffraction of single-crystalline Si (B_3) while planes from polycrystalline Si (B_1) originate rings of dots. The rest of the dispersed dots (from B_1 and/or B_2) were indexed considering the lattice spacing of phases related to Si, N and C combinations, thus taking into account the structures of Si, SiC cubic (3C) and hexagonal (2H, 4H, 6H and 8H) polytypes, Si_3N_4 (α and β) and C_3N_4 (β). The spot labelled as 'α' corresponds to α-Si_3N_4 for a lattice parameter of 0.179 ± 0.003 nm associated to (1 3 1) planes (real spacing: 0.1770 nm) or to (3 3 1) planes (real spacing: 0.1805 nm). The rest of the spots encircled in the figure cannot be assigned to a single phase but undoubtedly do not correspond to Si inclusions. For example, the spots labelled as X_a corresponds to a lattice spacing of 0.140 ± 0.003 nm. This parameter is assignable to different planes of hexagonal SiC (2H, 4H, 6H or 8H) or Si_3N_4 (α or β). Acting in this way, X_b is proposed to be originated by 8H-SiC or Si_3N_4 (α or β);

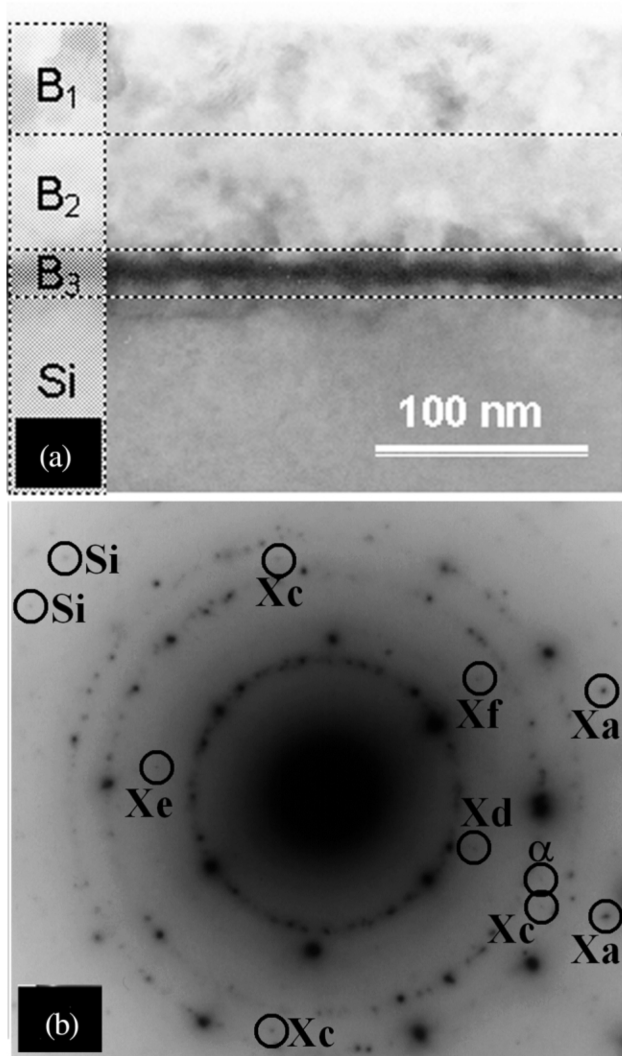

Fig. 5. Sample B characterization. (a) XTEM image of sample B showing layers B_1 (82 nm), B_2 (85 nm) and B_3 (22 nm). (b) SAED pattern registered along [1 $\bar{1}$ 0] of the Si substrate and layers B_1, B_2 and B_3. Concerning layers B_1 and B_2, spot 'α' is due to α-Si_3N_4, the dispersed dots labelled as X_a, X_c, X_d and X_e corresponds to SiC or Si_3N_4 or C_3N_4 misoriented new phases while Si inclusions are also detected.

X_d corresponds to hexagonal SiC (4H, 6H or 8H) or α-Si_3N_4; X_e corresponds to SiC (8H or 3C), β-Si_3N_4 or β-C_3N_4 and X_f corresponds 6H-SiC or one of the phases proposed for X_e. There are other isolated spots assignable only to the diffraction of Si inclusions into layers B_1 or B_2.

HREM images from layer B_1 and near the B_1/B_2 interface allow us to corroborate the presence of the inclusions detected by SAED experiments. Fig. 6a shows a HREM image of layer B_1 where (1 1 1)Si planes and Moiré fringes, that result from the superposition of (1 1 1)Si and crystalline inclusion planes, are indicated. The analyses of these Moiré patterns were carried out in order to detect the nature and the misorientation of the inclusions with respect to the Si matrix [13]. The small relative twist between grains and the substrate (α) could be calculated from Eq. (1)

$$D_{\mathrm{MOIRE}}=\frac{d_{\mathrm{Si}}d_{\mathrm{INCL}}}{\sqrt{d_{\mathrm{Si}}^2-d_{\mathrm{INCL}}^2-2d_{\mathrm{Si}}d_{\mathrm{INCL}}\cos(\alpha)}} \tag{1}$$

where d_{Si} represents the (1 1 1)Si planes spacing, d_{INCL} represents the inclusion planes spacing and $D_{\mathrm{MOIRÉ}}$ represents the Moiré fringes spacing. This real twist (α) is associated to the angle of rotation between the Moiré

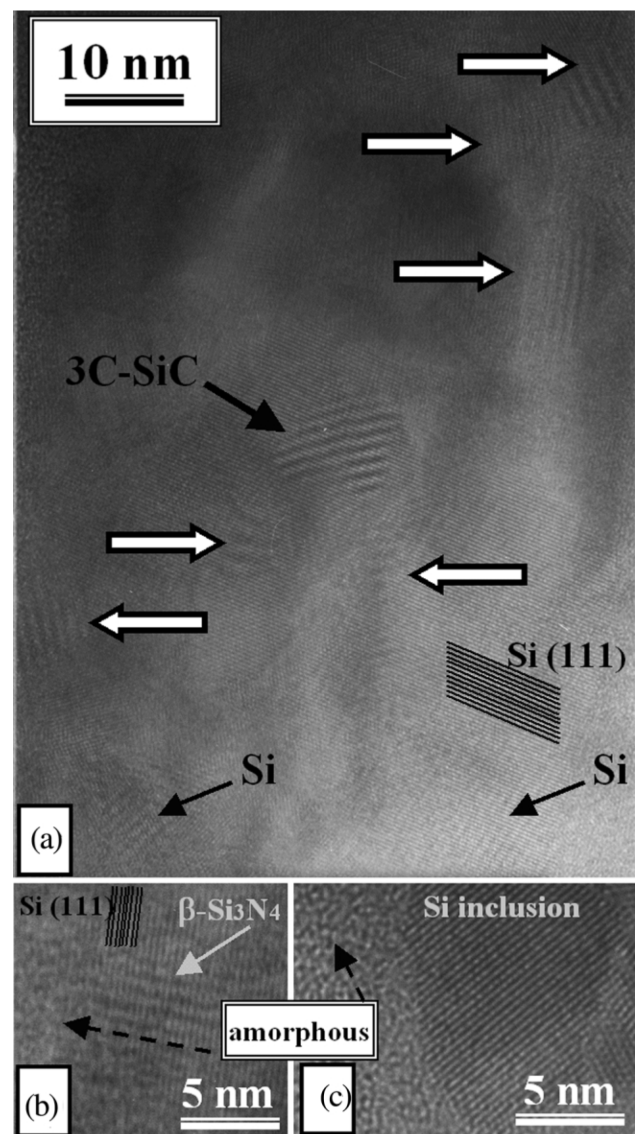

Fig. 6. HREM image of sample B. (a) Moiré contrasts located inside layer B_1 due to Si, 3C-SiC and other inclusions not being Si (white arrows point out SiC or Si_3N_4 or C_3N_4 inclusions). (b) Moiré promoted by a β-Si_3N_4 inclusion just near layer B_2. (c) Si inclusion placed inside amorphous layer B_2.

fringes and the substrate fringes in the image (β) by Eq. (2).

$$\sin(\beta)=\frac{d_{Si}\sin(\alpha)}{\sqrt{d_{Si}^2-d_{INCL}^2-2d_{Si}d_{INCL}\cos(\alpha)}} \quad (2)$$

From our HREM/MOIRÉ images some of the fixed parameters related to the inclusions such as $D_{MOIRÉ}$ and β can be measured using $d_{Si}=0.3130$ nm as reference spacing. Thus, using a fitting system of two equations with two variables, the parameters α and d_{INCL} are extracted. The parameter d_{INCL} is compared to the plane spacing of possible new phases. We have to note that in these careful analyses, the parameter of the polycrystalline Si in layer B_1 matrix is assumed to be relaxed. This fact is supposed after the comparison with respect to lattices measured inside the relaxed single-crystalline Si (far away from the strained surface and below layer B_3). The measurements of spacing and angles in the HREM images were carried out using the fast Fourier transform of the Moiré contrast region and the error was estimated to be approximately ±0.0500 nm for $D_{MOIRÉ}$ and ±1° for β, having an influence in the calculated values of ±0.0025 nm for d_{INCL} and ±1° for α.

Many inclusions cannot be assigned to a single phase again but the majority of them are clearly not related to polycrystalline Si. In this way, the Moiré's fringes marked with an arrow in Fig. 6a and a lot of inclusions for similar regions, indexed for SiC, Si_3N_4 and/or C_3N_4. The Moiré contrasts labelled as 'Si' in the figure correspond to (1 1 1)Si planes rotated 18° with respect to (1 1 1)Si foundation planes. For the inclusion labelled as '3C-SiC' in Fig. 6a, the Moiré pattern is originated by a grid of planes spaced 0.252±0.002 nm and rotated approximately 7° with respect to the (1 1 1)Si planes of the matrix. These planes are most probably the (1 1 1) planes of 3C-SiC showing a logical small strain since its parameter is 0.2511 nm in relaxed state. The inclusion of Fig. 6b was detected very near to layer B_2 and it is proposed to be due to β-Si_3N_4 because a grid spaced 0.293±0.002 nm (like (0 0 1) planes of β-Si_3N_4) and 23° rotated promotes this Moiré effect. HREM images of layer B_2 show that Si grains are contained into an amorphous matrix, as that shown in Fig. 6c, but inclusions of other nature were not detected by this technique. All the inclusions of new phases detected in sample B show irregular shapes spreading to elliptic forms with sizes from 18 to 170 nm^2. The average size of inclusions is 50 nm^2. Concerning the coherency of new phases with respect to the matrix, the detected planes are almost aligned in some cases and very rotated in other situations.

3.3. Sample C

In this sample the ion milling resistance during XTEM specimen preparation was higher than in samples A and B at the area affected by implantation near the surface. This fact denotes the higher hardness that the implanted region possesses in relation to the Si non-affected substrate. XTEM images registered along [1 $\bar{1}$ 0] zone axis let the visualization of three different layers (labelled as C_1, C_2 and C_3 in the XTEM image of Fig. 7. Layer C_1 thickness (measured by XTEM) is 26 (±2) nm. Layer C_2 thickness is 61 (±1) nm while layer C_3 is 125 (±5) nm.

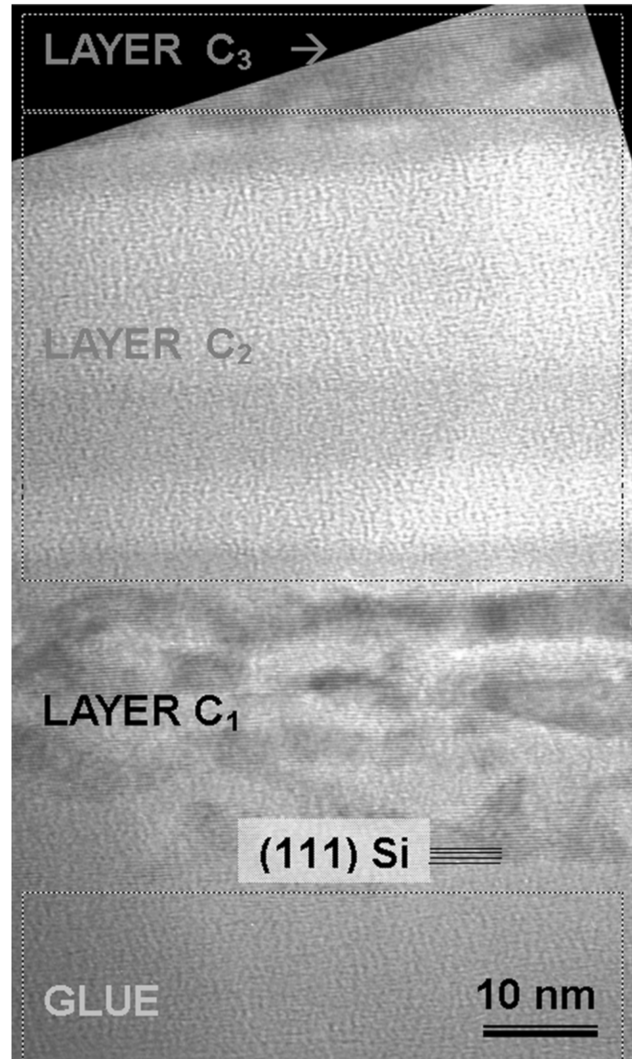

Fig. 7. HREM image of layers C_1 (well-aligned Si into amorphous: 26 nm), C_2 (amorphous: 61 nm) and the upper part of layer C_3 (single-crystalline Si with a darker contrast than the rest of the substrate: 125 nm).

SAED patterns for layers C_1, C_2 and C_3 were registered in XTEM and PVTEM preparations of sample C. Layer C_1 mainly consists of Si crystallites included inside an amorphous matrix. These Si crystallites are perfectly oriented with the (1 1 1)Si substrate material. Layer C_2 shows an amorphous nature while C_3 is Si single-crystal in the same orientation than the substrate

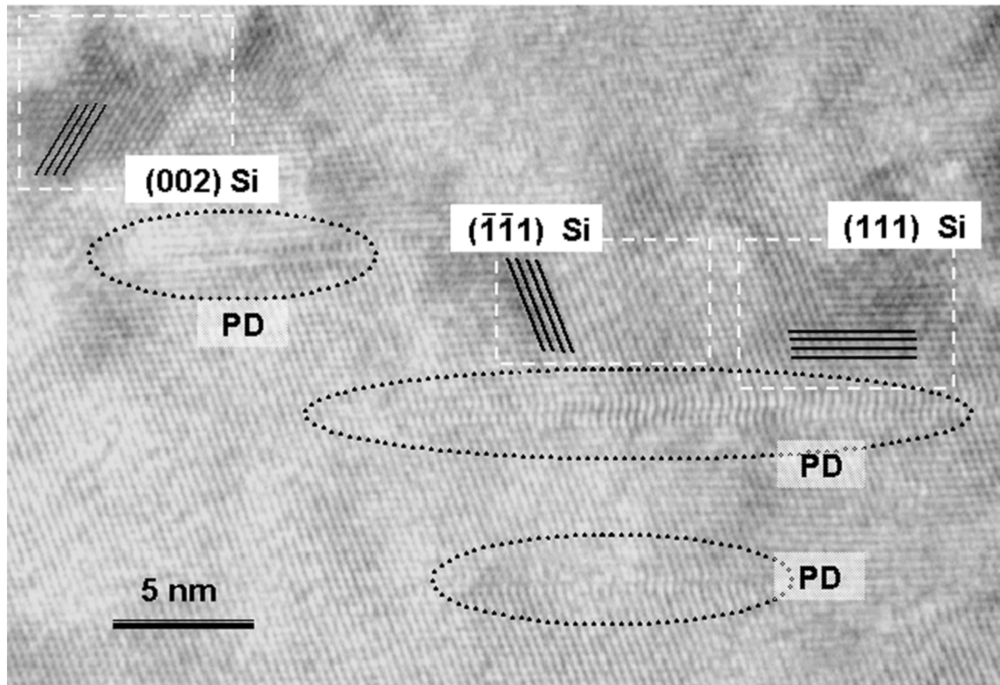

Fig. 8. HREM image of layer C_3. The ellipses surround PD and three different plane families of {1 1 1}Si are shown and labelled.

but showing a darker contrast in bright field TEM image mode.

Analyses of SAED patterns show that the Si present at region C_1 always has the same orientation than the silicon substrate. SAED patterns of layer C_2 from big regions and registered at long exposition times showed only the transmitted axis indicating the amorphous nature of C_2 while SAED patterns of region C_3 are identical to the diffraction shown by the deepest substrate. The electron diffraction of the three layers altogether in XTEM and PVTEM samples corresponded only to single-crystalline Si without extra spots in patterns. This fact indicates neither existence of crystalline structures related to combinations between Si atoms of the network and the implanted atoms nor polycrystallinity in the silicon itself.

In the HREM image of layers C_1, C_2 and the upper part of layer C_3 region shown in Fig. 7, crystallites with the same orientation and contained in an amorphous matrix are detected in layer C_1. These crystals exhibit fringes corresponding to (1 1 1)Si planes (parallel to Si substrate surface) and have regularly elongated shapes in the direction parallel to the surface with sizes that oscillated between 20 and 200 nm^2 and lengths from units to tens of nanometer. The detection of any crystalline structure was not possible in the amorphous layer C_2. This fact is in agreement with the observed results by SAED analysis. (1 1 1)Si planes, but without the amorphous discontinuity shown in C_1, are observed in HREM images of layer C_3.

The aspect of the transition between an amorphous area with a continuous contrast and a single-crystalline area with a very heterogeneous contrast is displayed in HREM images of C_2/C_3 interface. Fig. 8 shows a [1 $\bar{1}$ 0] HREM image of layer C_3 where several planar defects (PD) are visible. These defects are labelled and embraced inside ellipses in this image.

A dislocation study of sample C showed that there were not extended dislocations present in this sample. The $g \cdot b$ criterium with reflections 2 2 0, 1 1 1, 1 1 $\bar{1}$ and 0 0 2 was followed to make the latter asseveration.

3.4. Sample D

Three well-defined layers (D_1, D_2 and D_3) are evidenced again in the XTEM micrographs of sample D as it is shown in Fig. 9. The thickness measured on XTEM is 25.5 ($\pm$1.5) nm for layer D_1, 67.5 ($\pm$2.5) nm for layer D_2 and 45 ($\pm$3) nm for layer D_3. The graded change of contrast in layer D_2 in the XTEM image of Fig. 9 is due to a graded change of the TEM specimen thickness. However, layer D_2 is found to be amorphous in the region catalogued as D_2. From cross-sectional TEM and SAED of layers D_1 and D_3, the distribution of well-oriented Si in these layers is found to be almost analogous to that found in layers C_1 and C_3 in sample C but layer D_1 contains less amorphized regions and well-aligned inclusions of new phases inside it.

HREM images from layer D_1 allow to visualize Moiré contrasts due to new phases inclusions and the ($\bar{1}$ $\bar{1}$ 1)

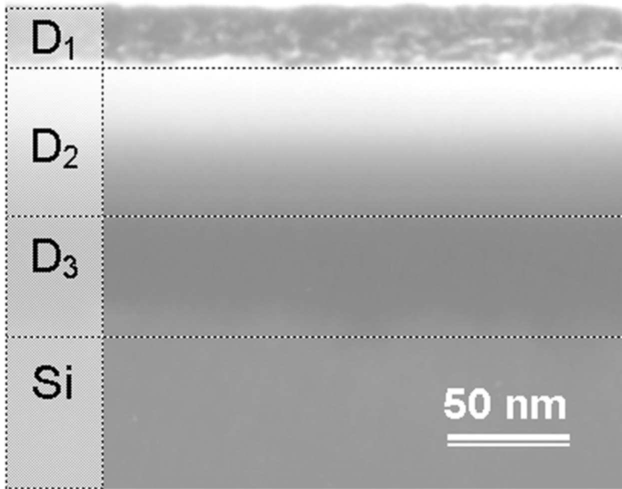

Fig. 9. XTEM image of buried layers in sample D. These layers have an average measured thickness from XTEM images of 25 nm for D_1, 67 nm for D_2 and 45 nm for D_3.

Si planes. Fig. 10 shows a cross-sectional HREM image with some Moiré contrasts undoubtedly not due to Si inclusions in layer D_1. The Moiré analysis permits to deduce that the inclusions labelled as X_1, X_2 and X_3 are due to β-C_3N_4 or 8H-SiC, and Y_1 and Y_2 are probably due to 3C-SiC or 6H-SiC and Y_3 could be β-Si_3N_4, 3C or 6H-SiC. The Moiré Z_1 belongs possibly to α-Si_3N_4 or to some of the 2H, 4H and 6H SiC polytypes. Table 2 shows the lattice parameter (d_2) that promotes the Moirés in each case of Fig. 10 and the angle of rotation between the substrate (Si (1 1 1) planes) and the planes belonging to the new phases. Measured misorientations for the new phases were less than 10° with respect to the substrate while the size of inclusions oscillated between 29.7 and 100.4 nm^2. Some of the inclusions are elongated and others show a circular shape but this behaviour seems not to be related to the misorientation or the character of the new phase. Size and long and short distances measured from near and distant ends of the inclusion's shapes are also shown in Table 2 linked to Fig. 10.

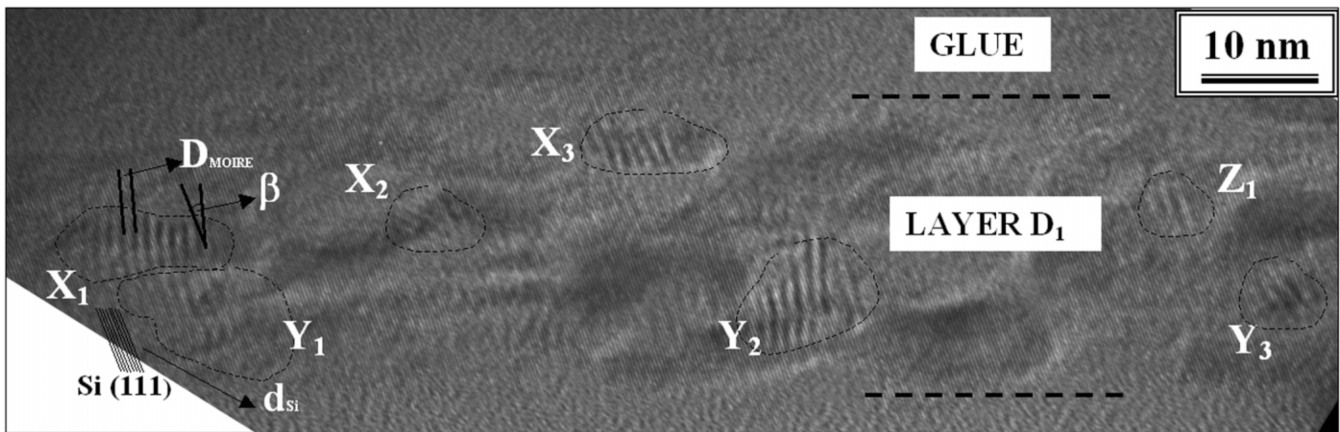

Fig. 10. XTEM/HREM image of layer D_1. The inclusions placed at this layer do not correspond to Si and its main features and the parameters measured and used for the subsequent Moiré analysis are listed in the attached table. All these planes are almost aligned (<10° rotated) with respect to the (1 1 1)Si foundation planes from the substrate.

Table 2
Main features and parameters used in the Moiré analysis associated to Fig. 10

Inclusion	D_{MOIRE} (±0.050 nm)	β (±1)	d_2 (±0.0025 nm)	α (±1)	Size (nm^2)	L (long) (nm)	L (short) (nm)	New phases (plane assignation)
X_1	1.121	−15.5	0.2463	−3.6	63.5	16.0	3.8	(0 0 1) β-C_3N_4: 0.2460 nm
X_2	0.945	40.0	0.2464	9.7	29.7	6.5	5.4	(1 0 3) 8H-SiC: 0.2469 nm
X_3	1.137	3.7	0.2455	0.7	54.5	13.6	4.5	
Y_1	1.285	4.7	0.2518	0.9	97.3	20.0	6.0	(1 1 1) 3C-SiC: 0.2511 nm
Y_2	1.269	−14.5	0.2523	−2.8	100.4	11.6	10.1	(1 0 2) 6H-SiC: 0.2516 nm
Y_3	1.205	16.3	0.2499	3.1	46.6	8.9	7.1	(1 2 0) β-Si_3N_4: 02490 nm
Z_1	1.407	−1.3	0.2561	−0.2	33.7	7.9	5.6	2H/4H/6H-SiC: 0.2570 nm (1 2 0) α-Si_3N_4: 0.2542 nm

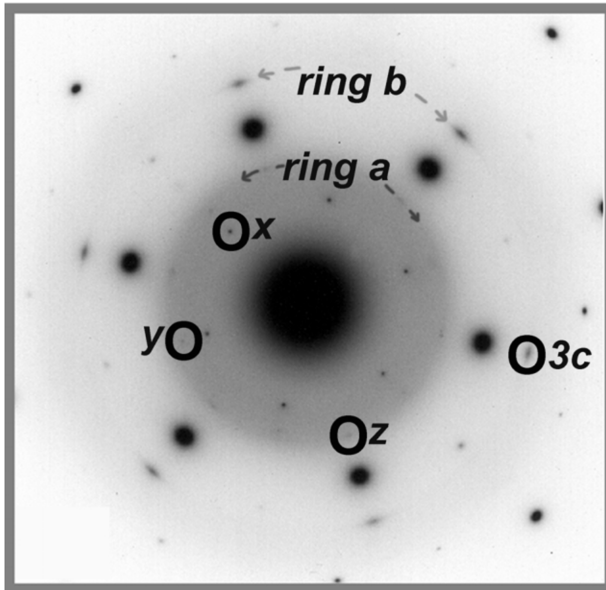

Fig. 11. SAED pattern registered along [0 0 1] of layers D_1, D_2 and D_3 from a PVTEM preparation of sample D. The image contrast is inverted for better visualization of 'x', 'y', 'z' and '3c' spots and rings 'a' and 'c'. The assignation of all these spots are related to well-oriented 3C-SiC (3c) and probably Si_3N_4 (x and z) and/or C_3N_4 or hexagonal SiC (y and z).

From the Moiré results, the existence of inclusions (other than Si) in layer D_1 is confirmed even though their exact crystalline nature cannot be confirmed. In order to identify the nature of such inclusions a detailed SAED analysis was carried out. Crystalline inclusions other than Si were detected from plan view SAED patterns of this sample. Fig. 11 shows a plan view SAED pattern of the whole three layers and the Si substrate. The contrast of this pattern is inverted to allow an easy visualization of the information included in it. Diffraction spots due to the Si substrate and Si from layer D_3 coincide with Si spots of layer D_1. This observation agrees with cross-sectional SAED and TEM studies of this sample. In addition to the main spots assigned to monocrystalline Si, four different families of diffraction spots, labelled as 'x', 'y', 'z' and '3c' in the SAED pattern of Fig. 11 ordered from the lowest to the highest diffraction vector (g), were detected.

These spots families were indexed using the EMS software considering binary crystalline phases formed between Si, C and/or N. Spots 'x' have two possible solutions for [0 0 1] zone axes of α-Si_3N_4 or β-Si_3N_4, although these spots could correspond to the forbidden {4/3 2/3 2/3} type reflections of Si, appearing when the density of PD parallel to the (1 1 1) plane is very high or due to the existence of a non-continuous Si lattice. Spots 'y' indexed assuming the [0 0 1] zone axis of β-C_3N_4 or [0 0 1] zone axes from hexagonal (2H, 4H, 6H and 8H) SiC polytypes. Spots 'z' indexed for various solutions: (i) α- and β-Si_3N_4 in [0 0 1] zone axis (most probable), (ii) β-C_3N_4 [0 0 1] zone axis and (iii) hexagonal SiC polytypes. Points labelled as '3c' are assigned to β-SiC in [1 1 1] zone axis and are totally aligned with (1 1 1)Si spots in [1 1 1] zone axis. Arcs in spots '3c' and 'z' denote that some of these inclusions are some degrees rotated to the matrix.

Plan view SAED pattern of Fig. 11 presents a couple of weak rings, labelled as rings 'a' and 'b'. These rings are associated to the presence of some few and small polycrystalline grains immerse in the implanted layers. The disperse intensity around these rings can also be associated with the presence of pseudo-amorphous material in an intermediate state of transformation towards the formed crystals. Identified polycrystalline and/or pseudo-amorphous material are likely to be associated to crystals corresponding to spots 'y' and/or 'z' (β-Si_3N_4, α-Si_3N_4, hexagonal SiC and/or β-C_3N_4) for ring 'a', and β-SiC for ring 'b'.

Fig. 12 shows four dark field (DF) images of sample D in PVTEM. This technique allows the visualization (in form of bright contrasts) of the dispersed crystalline grains of different phases into the structure. Fig. 12a and c are DF images obtained with the $2\,\bar{2}\,0$ reflection of Si, Fig. 12b is a DF image obtained with the same $2\,\bar{2}\,0$ reflection of β-SiC in the same area than in Fig. 12a while Fig. 12d is a DF image obtained with the first vector of diffraction of 'x'. Some isolated β-SiC grains are detected and encircled in the image of Fig. 12b. The bright features of Fig. 12d are due to [0 0 1]Si_3N_4, the discontinuous Si lattice and/or overlapping PD.

Dislocations that penetrated 600–700 nm inside the substrate from the inner interface of layer D_3 were occasionally detected. There were some other extended contrasts, less long and tangled, penetrating 200−300 nm under layer D_3 and also associated to dislocations. These features are shown in the two beam XTEM image of Fig. 13, registered with reflection 2 2 0 near the $[1\,\bar{1}\,0]$ zone axis.

4. Discussion

Fig. 14 is a schematic summary of the studied samples where the thickness and main structural features of layers formed after implantation/annealing are noted. SEM analyses of surface morphology of samples A–D show planar surfaces in contrast to some results previously described where 10 keV $^{15}N_2^+$ implantation at RT in (1 0 0)Si and doses from 0.5 to 5×10^{17} at. cm^{-2} resulted in the formation of roughness and surface whiskers of tens of nanometers that became more pronounced when annealing temperatures increased [42].

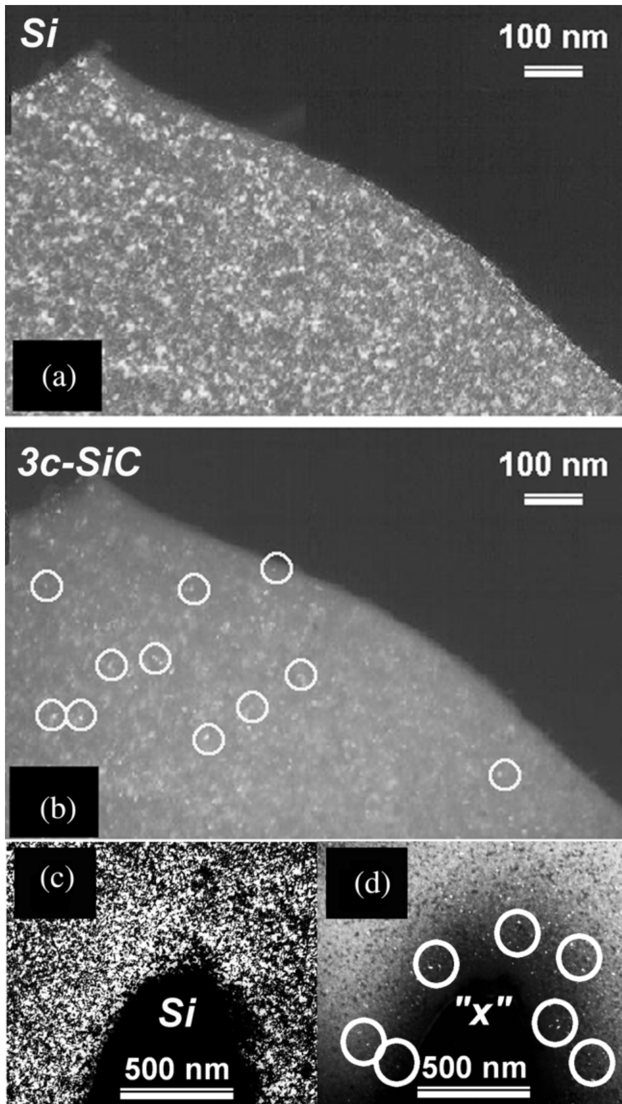

Fig. 12. Four DF images of sample D in the same region of a PVTEM preparation. (a) and (c) DF images obtained with the $2\,\bar{2}\,0$ reflection of Si. (b) DF image obtained with the $2\,\bar{2}\,0$ reflection of 3C-SiC where some dispersed 3C-SiC grains are encircled. (d) DF image obtained with the first vector of reflection of 'x'.

4.1. Implantations at room temperature

The presence of a polycrystalline α- and β-Si_3N_4 buried layer in layer A_2 of sample A agrees with the early theory of Pavlov [43]. N implantation in Si generates a solid-state chemical reaction, which forms Si_3N_4, promoted by radiation-induced defects. The only possible fragments formations are columns of SiN_4 tetrahedral characteristics of α-Si_3N_4 because the structure of Si governs the mechanism. Although the transition temperature from α- to β-Si_3N_4 is 1450 °C, annealing of the implanted samples leads to the appearance of polycrystalline α and β mixture at lower temperatures (1200 °C for sample A) than the transition temperature, by means of a mechanism of resonance jumps of silicon atoms. Such mechanism explains that the formation of Si_3N_4 precipitates, recovery of the disturbed structure and emission of mobile point defects accompany precipitation of a supersaturated solution of N in Si during annealing [44]. The α plus β-Si_3N_4 mixture behaviour was shown in the N ion implantation literature [3,43,45–47] though the exclusive presence of polycrystalline α-Si_3N_4 without β-Si_3N_4 was reported in some other works. The existence of α-Si_3N_4 without β-Si_3N_4 occurred at RT 2.5 and 7.5×10^{17} cm^{-2} of N^+ and 200 keV plus 1200 °C annealing [48], at RT 14×10^{17} cm^{-2} of $^{15}N^+$ and 200 keV plus 1200 °C/2 h annealing [49], at 500 °C from 1 to 10×10^{17} cm^{-2} of N^+ and N_2^+ and 95 keV plus 1200 °C/2 h annealing [50] and in the presence of Fe atoms [51]. We have to note that the latter α buried layers (in an amorphous matrix) were produced at equivalent doses but higher energies (medium ion implantation energies) than those used in our case. In this way the literature only reports about Si_3N_4, Si–N bonds or stoichiometric mixtures in most cases without focusing on the crystallographic character of the phases formed.

Sample A showed a small reduction in the lattice parameter in the nearest surface region [39] that denotes the emplacement of N atoms at substitutional sites after annealing. This negative strain (of contraction) was shown in N^+ implantation of Si at similar doses but at higher temperature of implantation in a practically damage-free Si over-layer [52,53]. However, we have to take into account that (i) the formation of nitride precipitates is associated with a volume increase of 0.004 nm^3 per Si atom [38] and (ii) the amount of N^+ implanted in our samples was over the solubility limit of N in Si and could create positive strain (volume increase by interstitial N) and formation of amorphous Si_3N_4 buried layers. The amorphous phase in A_2 appeared because the N implanted was also well over the critical amorphization dose. The same amorphization appeared in other N implantation experiments normally

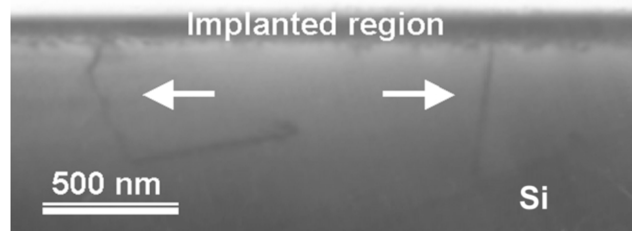

Fig. 13. Two beam XTEM images of sample D registered with reflection 2 2 0 near $[1\,\bar{1}\,0]$ zone axis. Tangled contrasts just under the implanted region are due to small dislocations while two long dislocations penetrating hundreds of nanometers inside the substrate are pointed with arrows.

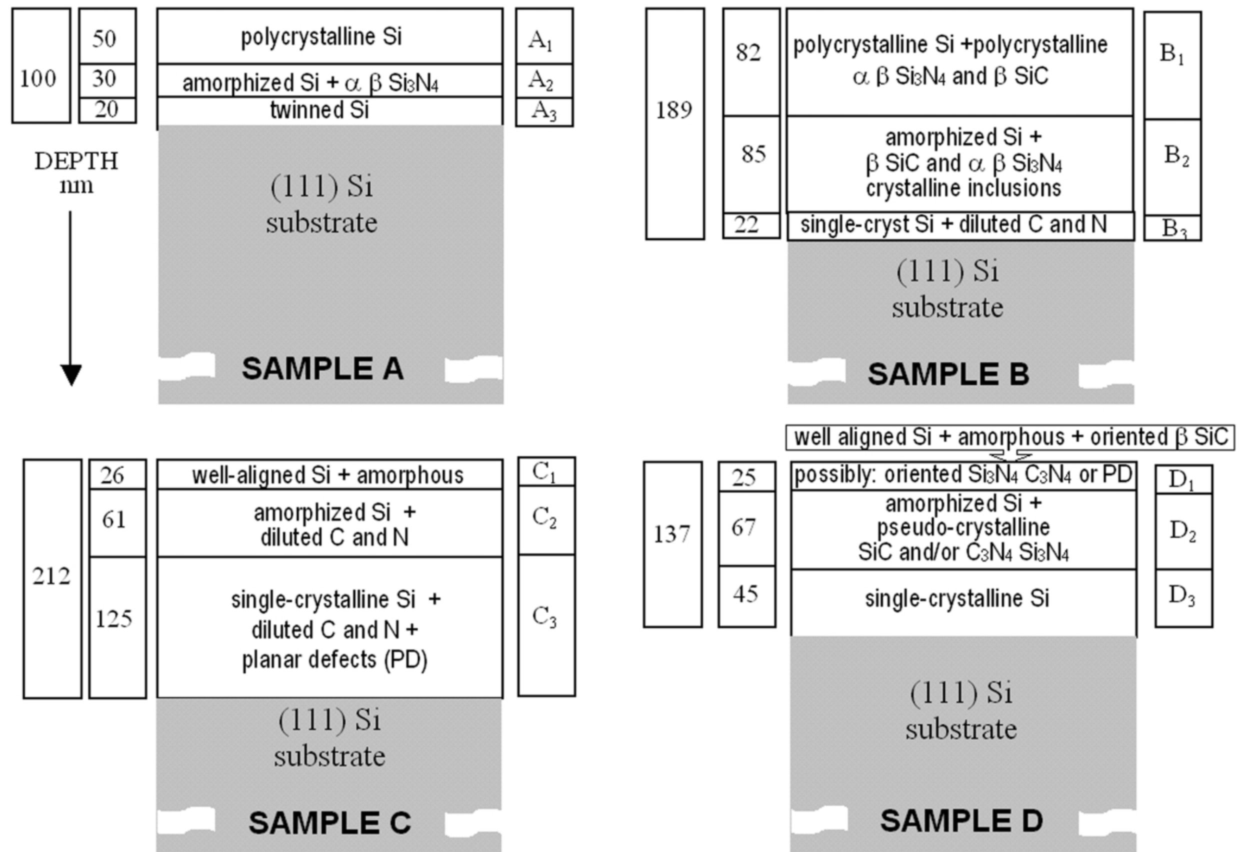

Fig. 14. Schematic summary of layers structure and thickness of samples A, B, C and D.

before annealing [48,51] and occasionally after annealing [54,55]. Microtwins at region A_3 were described as a defect induced by N implantation [48] and the presence of heavily damaged regions in the back interface of the nitride layer with the underlying Si was shown in N implantation at RT after annealing [49,56].

Sample B has a similar behaviour to A, but effects of carbon implantation results in a longer depth distribution of the region affected and in the appearance of phases with Si and C atoms combinations. Polycrystalline inclusions of Si, α-Si_3N_4, β-Si_3N_4 and β-SiC were detected in regions B_1 and B_2. The presence of hexagonal SiC new phases in B_1 and B_2 cannot be unambiguously confirmed but some diffraction spots in our SAED experiments could be originated by 2H, 4H, 6H or 8H-SiC. Nitride components appearance was cleared before. Carbide mix was observed by some researchers in RT C^+ implantation of Si [57,58]. Normally in the as-implanted state Si–C bonds are detected forming microregions of SiC, which may be crystallites of α-SiC or amorphous SiC clusters. At anneal temperatures in the range of 800–900 °C, depending on the implantation conditions, a transition to β-SiC occurs as a result of both crystallization of the Si matrix, and misfit strain [38,59]. However, C does not easily segregate in a macroscopic scale during implantation or conventional annealing at 1200 °C and it is very resistant to migration because Si–C bonds formed have high value of activation energy for an effective segregation, much higher than the Si–N system. By this fact, C fixes in very small stationary SiC precipitates in a microscopic scale [60]. Some other researchers have found only β-SiC polytype after RT implantation and annealing [61]. Furthermore, they had found a significant dependence of β-SiC fraction in the as-implanted samples on the magnitude of the implantation energy used, for doses and implantation energies of the order used in this work. They attributed this fact to ion beam induced crystallization (IBIC) effects but much care was taken in order to avoid self-annealing effects in our samples A and B and the sample holder was maintained at RT by means of a closed cycle circuit during the implantation. Anyway, the evolution of the various SiC phases after annealing is well described by the classical nucleation and growth theory using a two-dimensional growth model. Contraction and expansion contributions of the network were detected in sample B [39]. Contraction is probably due to N and C disposition in substitutional sites of the Si lattice. Its lower masses facilitate the incorporation in substitutional (tetrahedral) sites and a

reduction in the bond length. This dilution could be the reason of the darker contrast showed by layer B_3. Other reasons of contraction after annealing are the rearrangement of displaced Si atoms and the so-called free-volume accommodation, because SiC formation leads to a volume reduction by a factor of approximately 2 [60]. Expansion effect is attributed to disorder and the formation of random metastable phases and anisotropic structures after annealing. Another reason is that 'interstitial' fraction of C and N atoms is still dominant after annealing in some places of the specimen layer structure [62]. The presence of affected Si regions under SiC buried layers was also shown in RT implantation of C after annealing [63].

The post-implantation annealing process was enough to transform the surface layers A_1 and B_1 into polycrystalline Si but not for annealing out all the amorphous phase of A_2 or B_2. Amorphization occurs at RT implantation by ionic impact onto the surface. A critical density of lattice disorder is built up or small discrete zones of damage (resulting from the overlap of individual collision cascades and subsequent relaxation of mobile point defects) accumulate and coalesce to form extended amorphous regions [11,38]. Silicon amorphization during ion implantation was also modelled as a thermal phenomenon where amorphizing single-recoil events and collision cascades were taken into account [64,65]. The early N^+ implantation gives rise to an amorphous surface layer in which C^+ is subsequently implanted. Furthermore, a critical concentration of C to amorphize the Si substrate was defined as 10^{21} cm^{-3} [66,67] while in our experiments the dose was chosen to obtain a concentration of implanted ions of approximately 5×10^{22} cm^{-3}, similar to the bulk Si density. Layers containing incorporated carbon in a metastable solubility limit of approximately 10^{20} cm^{-3} can be produced from interstitial carbon in appropriate conditions with doses lower than 10^{15}–10^{16} at. cm^{-2}. This is the critical amorphization dose for implantation energies in the range of that used in our case [68,69], while we used larger doses, in the 10^{17}–10^{18} at. cm^{-2} range. The use of these concentrations, besides the N^+ implantation, explains the remaining of amorphous zones upon annealing, and we think that higher temperatures or larger times of annealing are required to complete the recrystallization of the Si over-layers A_1 and B_1. Complete recrystallized top layers have not been found at RT and low energy implantation plus annealing conditions for C^+ or N^+ implantations. At medium energies, for instance, RT 100 keV and 1×10^{17} cm^{-2} C^+, 1000 °C annealing were enough to completely recrystallize a top layer consisting of a mixture of non-affected Si and amorphous Si–C [70]. At 150 keV a thin C-rich surface film attributed to a C migration towards the surface was formed before annealing [11]. In RT Si implantations at high energies (MeV), over-layers are normally single-crystalline and defect-free even without annealing because the nuclear energy deposited into surface regions is very low. Moreover, SiC polycrystalline over-layers were found in RT implantation into Si at 40 keV and 3.8×10^{17} cm^{-2} of $^{13}C^+$ before RTA annealing [58] and top Si_3N_4 layers have been also shown in N implantation experiments at RT plus annealing [71].

4.2. Implantations at high temperature (600 °C)

HT implantation at 600 °C is the main experimental feature of samples C and D. HT implantation allows self-annealing processes and enhanced diffusion of defects. Amorphization could be avoided although large damage complexes which often collapse to form extended defects can be created. At HT the formation of SiC and Si_3N_4 is favoured and the level of damage in the Si over-layer is reduced. There are not much attempts in the low energy range of work for nitrogen ions HT implantation using our doses range. However, there are much results for medium energies ($\approx$100–200 keV). Buried layers of amorphous Si_3N_4 and polycrystalline α phase mixtures before 2 or 8 h, 1200 °C annealing were reported for 500–520 °C implantations. These buried layers became single-crystalline when higher temperature annealing (1405 °C) were used while single-crystalline Si over-layers were described in all cases. Amorphous buried layers and affected Si over-layers were usual [48,50,54,72] before annealing. For higher temperatures of implantation (600–1100 °C), α-Si_3N_4 polycrystalline inclusions are developed directly at temperatures as high as 700 or 900 and 1000 °C is defined as the limit in which N is not retained by the Si network and migrates to the surface. Single-crystalline top Si layers are always showed in excess of 600 °C. Related to annealing, 1100–1200 °C is the transition temperature for the well-oriented emplacement of α-Si_3N_4 with respect to the matrix, although generally abrupt Si and Si_3N_4 interfaces are described [73]. Almost all the results reported for implantation doses carried out within the range used for us coincide with the use of medium and high energies for carbon ions HT implantations. At high substrate temperature during implantation, in situ redistribution of the implanted C occurred enabling the direct synthesis (without annealing) of a buried layer of well-aligned small β-SiC precipitates placed inside a single-crystalline Si matrix at 500 °C [9,11], 860 °C [10], 880 or 950 °C [2,13] and other intermediate temperatures. These buried layers are overlain by single-crystal Si whose quality is best for the highest temperature used and have extremely rough interface. HT implantation in the range of 400–600 °C and subsequent annealing was also used with similar results or sometimes showing an amorphous component [65]. To our knowledge, only two works showed 30–60 keV high-doses carbon implantation at substrate temperatures below 400 [59]

or up to 450 °C [74], and the conversion of amorphous SiC phase into β-SiC was also shown during the process of implantation. These results could help us to understand the results found in the characterized samples C and D. The creation of structural defects by subsurface accumulation of implanted ions is sometimes shown like centres of nucleation and growing of carbide or nitride phases [73].

A topotactic transition is a solid-state transformation imposed by the Si network where the product is structurally and orientationally related to the starting material [75]. This is the accepted model that explains that cubic SiC well aligned with respect to the matrix is the equilibrium structure of high-doses implanted samples after annealing or after HT implantations. Well orientation of SiC and probably C_3N_4 and Si_3N_4 crystallites phases included into a single-crystalline Si matrix make us think in a topotaxial disposition of the three elements in layer D_3. So we assume that carbon and nitrogen were partially dissolved occupying substitutional sites in the Si lattice in the early stage (layer C_3) and during annealing. Later on, it occurred a C and N migration towards the D_2/D_3 interface region that explains the difference of thickness between C_3 and D_3. Finally, Si, C and N combinations took place forming oriented compounds inside the network with the related volume changes. For example, a 48% local volume contraction is expected if a Si unit cell is replaced by a β-SiC unit cell in only C implantation but really there are four Si interstitial atoms (Si_i) emitted in the β-SiC formation process. These Si_i react with new carbon atoms that would originate two SiC unit cells per Si unit cell and a 3.25% of volume expansion [38]. The presence of N complicates these assumptions and Si–C, C–N and Si–N clusters play their roles in our experiments. Furthermore, incipient pseudo-aligned stays of these elements were likely to be present in the amorphous layer D_2 after annealing but not before annealing in layer C_2. This result contrasts with a publication [65] where the existence of aligned precipitates in depth zones surrounded by amorphous material is claimed to be due to precipitate formation prior to the onset of amorphization in Si implantation at 400–600 °C. After samples C and D comparison, it seems that in our samples undoubtedly amorphization was generated before other phase formations, that means (or allows to deduce) the precipitates formation into the amorphous layer is a result of annealing in sample D. In this way, authors who had direct synthesis of polycrystalline or well-aligned Si_3N_4 or SiC precipitates at moderate HT of implantation always used higher energies than those used for us and we think that the formation of precipitates was enhanced by the higher in situ annealing effects that IBIC promoted in their structures compared to ours.

Layers C_1 and D_1 are similar in composition showing single-crystalline Si inside an amorphized matrix. Although D_1 is in a more advanced stay of recrystallization than C_1, the complete change to single-crystalline Si was not possible after applying the annealing. These non-amorphized cubic Si regions are not completely strain relaxed [53,65]. A higher annealing temperature or more annealing time should be enough to complete the recrystallization as previously it was demonstrated in similar cases. HT implantation mode leads to the formation of a better non-defectuous top single-crystalline Si layer. The above-mentioned facts and thoughts lead to the following possible explanation. During the implantation some of the Si remains unaffected as one can see in layer C_1, the rest of the amorphized component contains N and C in excess that migrate to the amorphous buried layer or that react to form new phase inclusions during the advance of subsequent annealing. Thus the Si precursor will always lead to aligned clusters in the over-layer and will create a single-crystalline layer that will not be free of complete strain relaxation because the effect of its foundation (buried layer). The possible existence of the well-aligned Si_3N_4 and C_3N_4 inclusions in sample (D) supports the present hypothesis.

Two additional effects induced by annealing are the thickness reduction of zones affected by implantation and the generation of damage and occasional but large defects. Concerning changes of implanted layer thickness, the comparison between samples B, C and D demonstrates that there is a decrease in the zone affected after annealing and this contraction is more evident when HT implantation is used. Thus, in the non-annealed sample (C) the thickness of the zone affected by implantation is 212 nm, which is larger than in the other annealed samples. However, the HT pre-implanted sample (D) has an affected total zone thinner (137 nm) than the RT implanted sample (198 nm). Detailed focus on sample sublayers demonstrates that the single-crystalline deepest layer (the darkest in on-axis images) suffers the largest change of thickness with annealing. Comparing samples C and D, where annealing is the only difference, thickness from C_3 to D_3 tends to decrease while from C_2 to D_2 and from C_1 to D_1 thickness remains almost constant. Similar variations of thickness with annealing were previously shown in N ion implantation [5,76,77] and C ion implantation [4,65,78]. The implanted atoms redistribute and deplete preferably to the amorphous N-rich or C-rich layer from the top layer or from the inner layer creating a box-like depth distribution during the heat treatment. Related to the defects that appeared, stacking faults, microtwins and dislocations are common defects morphologies that arise during HT, C or N implantation and also after annealing [13,48,49,52,53,69]. In most cases, when both small and large defects are present simultaneously in a structure, heat treatments usually help further growth of large defects and reduce the amount of the small ones [79]. That occurred in sample D where dispersed but

large dislocation loops appeared, like the reported in other N [80] or C [17] implantations. These loops seem to have electric properties and can act to store interstitial for prolonged periods of anneal creating supersaturation and TED.

5. Conclusion

A deep TEM structural study of N^+ and C^+ implantation in Si substrates at 30 keV is presented. An enhancement in the crystalline quality of buried and top layers created by $C^+ + N^+$ implantation is demonstrated by means of subsequent annealing, HT implantation, or better, by applying the simultaneous combination of both processes.

A buried layer of well-oriented crystalline inclusions of SiC and probably C_3N_4 and Si_3N_4 into a well-oriented Si matrix was synthesized by heavy dose $C^+ + N^+$ implantation into silicon at a temperature of 600 °C and subsequent annealing at 1200 °C for 2 h. The implanted Si at 600 °C both with further and without subsequent annealing at 1200 °C for 2 h has a thin (∼25 nm) well-oriented Si over-layer with an amorphous component.

These are promising results for the use of ion implantation to obtain stoichiometric oriented crystalline thin layers.

Acknowledgments

This work has been financed for the Spanish MCYT through the projects MAT98-0823-C03-02/03 and MAT2000-0478-94-02 and the Junta de Andalucía (Group TEP-0120). TEM measurements were carried at the 'División de Microscopía Electrónica, SCCYT, Universidad de Cádiz'. One of the authors, F.M. Morales, would like to thank G. Aragón for his economic support and F. León by the collaboration in TEM sample preparation. We also thank P. Rodríguez for ion implantation of the samples.

References

[1] Z.T. Kuznicki, J.J. Grob, B. Prevot, Nucl. Instrum. Methods Phys. Res. B 112 (1996) 188.
[2] C.-L. Lin, J.-H. Li, S.-K. Zhang, Y.-H. Yu, Z.-C. Zou, Nucl. Instrum. Methods Phys. Res. B 55 (1991) 742.
[3] M.C. Poon, Y.W. Lam, S.P. Wong, Semicond. Sci. Technol. 7 (1992) 414.
[4] Q.-Y. Tong, H.-M. You, G. Cha, U. Gösele, Appl. Phys. Lett. 62 (1993) 970.
[5] Z.-Y. Shi, C.-L. Lin, W.-H. Zhu, P.L.F. Hemment, U. Bussmann, S.C. Zou, Nucl. Instrum. Methods Phys. Res. B 74 (1993) 210.
[6] J.P. Colinge, V.S. Lisenkov, A.N. Nayarov (Eds.), Physical and Technological Problems of SOI Structures and Devices, NATO ASI Series, Kluwer, New York, 1995.
[7] S. Zappe, E. Obermeier, J. Stoemenos, H. Moller, G. Krotz, H. With, W. Skorupa, Mater. Sci. Eng. B 61 (1999) 522.
[8] C. Serre, A. Pérez-Rodríguez, J.R. Morante, J. Esteve, M.C. Acero, R. Kögler, W. Skorupa, J. Microelectromech. Microeng. 10 (2000) 152.
[9] A. Romano-Rodríguez, A. Pérez-Rodríguez, C. Serre, J.R. Morante, J. Esteve, M.C. Acero, R. Kögler, W. Skorupa, M. Östling, N. Nordell, S. Karlsson, J. Van Landuyt, Silicon Carbide and Related Materials-1999 PTS, 1&2 Materials Science Forum, 338-3 (2000) 309.
[10] P. Martin, B. Daudin, M. Dupuy, A. Ermolieff, M. Olivier, A.M. Papon, G. Rolland, J. Appl. Phys. 67 (1990) 2908.
[11] C. Serre, A. Pérez-Rodríguez, A. Romano-Rodríguez, J.R. Morante, R. Kögler, W. Skorupa, J. Appl. Phys. 77 (1995) 2978.
[12] A. Nejim, P.L.F. Hemment, J. Stoemenos, Appl. Phys. Lett. 66 (1995) 2646.
[13] N. Frangis, J. Stoemenos, J. Van Landuit, A. Nejim, P.L.F. Hemment, J. Cryst. Growth 181 (1997) 218.
[14] S.I. Molina, F.M. Morales, D. Araújo, Mater. Sci. Eng. B 80 (2001) 342.
[15] C. Serre, A. Pérez-Rodríguez, A. Romano-Rodríguez, L. Calvo-Barrio, J.R. Morante, J. Esteve, M.C. Acero, R. Kögler, W. Skorupa, J. Electrochem. Soc. 144 (1997) 2212.
[16] P.A. Stolk, D.J. Eaglesham, H.-J. Gossmann, J.M. Poate, Appl. Phys. Lett. 66 (1995) 1370.
[17] A.H. Gencer, S.T. Dunham, in: D.E. Alexander, N.-W. Cheung, B. Park, W. Skorupa (Eds.), Quantitative analysis of chemically-enhanced sputtering during ion beam deposition of carbon nitride thin films, materials modification and synthesis by ion beam processing, Boston, USA, December 2–6, 1996, Materials Research Society Symposium Proceedings 438 (1997) 27.
[18] S.M. Hu, R.O. Schwenker, J. Appl. Phys. 49 (1978) 3259.
[19] I.G. Stoev, R.A. Yankov, C. Yeines, Sensors Actuators 19 (1989) 183.
[20] A. Markwitz, M. Arps, H. Baumann, E.F. Krimmel, K. Bethge, Nucl. Instrum. Methods Phys. Res. B 113 (1996) 223.
[21] P. Berruyer, M. Bruel, Appl. Phys. Lett. 50 (1987) 89.
[22] C.-Y. Kang, W.-J. Cho, D.-G. Kang, Y.-J. Lee, J.M. Hwang, Appl. Phys. Lett. 74 (1999) 1833.
[23] J.A. Diniz, A.P. Sotero, G.S. Lujan, P.J. Tatsch, J.W. Swart, Nucl. Instrum. Methods Phys. Res. B 166 (2000) 64.
[24] A. Markwitz, M. Arps, H. Baumann, G. Demortier, E.F. Krimmel, K. Bethge, Nucl. Instrum. Methods Phys. Res. B 124 (1997) 506.
[25] P. Kodall, M. Hawley, K.C. Walter, K. Hubbard, N. Yu, J.R. Tesmer, T.E. Levine, M. Nastasi, Wear 205 (1997) 144.
[26] A.J. Stevens, T. Koga, C.B. Agee, M.J. Aziz, C.M. Lieber, J. Am. Chem. Soc. 118 (1996) 10900.
[27] Z. Zhang, S. Fan, J. Huang, C.M. Lieber, Appl. Phys. Lett. 68 (1996) 2639.
[28] A.Y. Liu, M. Cohen, Science 245 (1989) 841.
[29] D.M. Teter, R.J. Hemley, Science 271 (1996) 53.
[30] I.H. Murzin, G.S. Tompa, J. Wie, V. Muratov, T.E. Fischer, V. Yakovlev, in: D.E. Alexander, N.-W. Cheung, B. Park, W. Skorupa (Eds.), Quantitative analysis of chemically-enhanced sputtering during ion beam deposition of carbon nitride thin films, materials modification and synthesis by ion beam processing, Boston, USA, December 2–6, 1996, Materials Research Society Symposium Proceedings 438 (1997) 569.
[31] H. Hofsass, C. Ronning, H. Feldermann, M. Sebastian, in: D.E. Alexander, N.-W. Cheung, B. Park, W. Skorupa (Eds.), Quantitative analysis of chemically-enhanced sputtering during ion beam deposition of carbon nitride thin films, materials modification and synthesis by ion beam processing, Boston, USA, December 2–6, 1996, Materials Research Society Symposium Proceedings, 438 (1997) 575.

[32] A. Hoffman, I. Gouzman, R. Brener, Appl. Phys. Lett. 64 (1994) 845.
[33] S.P. Withrow, J.M. Williams, S. Prawer, D. Barbara, J. Appl. Phys. 78 (1995) 3060.
[34] Y.-S. Gu, L.-Q. Pan, M.-X. Zhao, X.-R. Chang, Z.-Z. Tian, J.-M. Xiao, Chin. Phys. Lett. 13 (1996) 782.
[35] A. Nakao, M. Iwaki, H. Sakahiri, K. Terasima, Nucl. Instrum. Methods Phys. Res. B 65 (1992) 352.
[36] C. Ulsu, B. Park, D.B. Poker, J. Electron. Mat. 25 (1996) 23.
[37] L.B. Freund, W.D. Nix, Appl. Phys. Lett. 69 (1996) 173.
[38] W. Skorupa, R.A. Yankov, Mater. Chem. Phys. 44 (1996) 101.
[39] L. Barbadillo, M.J. Hernández, M. Cervera, P. Rodríguez, J. Piqueras, S.I. Molina, F.M. Morales, D. Araújo, Nucl. Instrum. Methods Phys. Res. B 184 (2001) 361.
[40] N. Laidani, M. Bonelli, A. Miotello, L. Guzman, L. Calliari, M. Elena, R. Bertoncello, A. Glisemti, R. Capelletti, P. Ossi, J. Appl. Phys. 74 (1993) 2013.
[41] S. Miyagawa, S. Nakao, K. Saitoh, M. Ikeyama, H. Niwa, S. Tanemura, Y. Miyagawa, K. Baba, J. Appl. Phys. 78 (1995) 7018.
[42] A. Markwitz, H. Baumann, E.F. Krimmel, K. Bethge, W. Grill, Appl. Phys. Lett. 64 (1994) 2652.
[43] P.V. Pavlov, Sov. Phys. Crystallogr. 24 (1979) 277.
[44] G.A. Kachurin, I.E. Tyschenko, Semiconductors 27 (1993) 658.
[45] E.A. Taft, J. Electrochem. Soc. 118 (1971) 1341.
[46] V.I. Belyi, L.L. Vasilyeva, A.S. Ginovker, V.A. Gritsenko, S.M. Repinski, S.P. Sinitsa, T.P. Smirnova, F.L. Edelman, Materials Science Monographs 34: Silicon Nitride in Electronics, Elsevier, Amsterdam, 1988, p. 138.
[47] L. Barbadillo, M.J. Hernández, M. Cervera, P. Rodríguez, J. Piqueras, J. Appl. Phys. 87 (2000) 8385.
[48] C.D. Meekison, G.R. Booker, K.J. Reeson, P.L.F. Hemment, R.F. Peart, R.J. Chater, J.A. Kilner, J.R. Davis, J. Appl. Phys. 69 (1991) 3503.
[49] E.C. Paloura, A. Ginoudi, A. Markwitz, C. Lioutas, M. Katsikini, K. Bethge, S. Aminpirooz, H. Rossner, E. Holub-Krappe, T. Zorba, D. Siapkas, Nucl. Instrum. Methods Phys. Res. B 113 (1996) 227.
[50] C.-L. Lin, J.-H. Li, S.-K. Zhang, Y.-H. Yu, S.-C. Zou, Nucl. Instrum. Methods Phys. Res. B 55 (1991) 742.
[51] Z.-L. Li, J. Wonng-Leung, P.N.K. Deenapanray, M. Conway, D.J. Chivers, J.D. FitzGerald, J.S. Williams, Nucl. Instrum. Methods Phys. Res. B 148 (1999) 534.
[52] J.P. de Souza, Y. Suprun-Belevich, H. Boudinov, C.A. Cima, J. Appl. Phys. 87 (2000) 8385.
[53] J.P. de Souza, Y. Suprun-Belevich, H. Boudinov, C.A. Cima, J. Appl. Phys. 89 (2001) 42.
[54] P.L.F. Hemment, R.F. Peart, M.F. Yao, K.G. Stephens, R.J. Chater, J.A. Kilner, D. Meekison, G.R. Booker, R.P. Arrowsmith, Appl. Phys. Lett. 46 (1985) 952.
[55] V.I. Bachurin, A.B. Churilov, E.V. Potapov, V.K. Smirnov, V.V. Makarov, A.B. Danilin, Nucl. Instrum. Methods Phys. Res. B 147 (1999) 316.
[56] A. Markwitz, H. Baumann, E.F. Krimmel, R.W. Michelmann, C. Maurer, E.C. Paloura, K. Bethge, Appl. Phys. A 59 (1994) 435.
[57] K.J. Reeson, J. Stoemenos, P.L.F. Hemment, Thin Solid Films 191 (1991) 147.
[58] E. Theodossiu, H. Baumann, M. Klimenkov, M. Matz, K. Bethge, Phys. Stat. Sol. A 182 (2000) 653.
[59] H. Yan, B. Wang, X.-M. Song, L.-W. Tan, S.-J. Zhang, G.-H. Chen, S.-P. Wong, R.W.M. Kwok, W.-M. Lau-Leo, Diamond. Relat. Mater. 9 (2000) 1795.
[60] U. Gösele, Mater. Res. Symp. Proc. 59 (1986) 419.
[61] D.-H. Chen, W.-Y. Cheung, S.-P. Wong, Nucl. Instrum. Methods Phys. Res. B 148 (1999) 589.
[62] S. Isomae, T. Ishiba, T. Ando, M. Tamura, J. Appl. Phys. 74 (1993) 3815.
[63] E. Theodossiu, H. Baumann, E.K. Polychroniadis, K. Bethge, Nucl. Instrum. Methods Phys. Res. B 161 (2000) 941.
[64] C.F. Cerefolini, L. Meda, Phys. Rev. B 36 (1987) 5131.
[65] J.K.N. Lindner, B. Stritzker, Nucl. Instrum. Methods Phys. Res. B 148 (1999) 528.
[66] H. Wong, J. Lou, N.W. Cheung, E.P. Kvam, K.M. Yu, D.A. Olson, J. Washburn, Appl. Phys. Lett. 57 (1990) 798.
[67] S. Chevacharoenkul, J. Ilzhoefer, D. Feijoo, U. Gösele, Appl. Phys. Lett. 58 (1991) 1434.
[68] J. Candelaria, J. Watanabe, N. Theodore, R. Gregory, D. Schroder, L. Stont, N. Cave, Mater. Res. Soc. Symp. Proc. 321 (1994) 472.
[69] J.W. Strane, S.R. Lee, H.J. Stein, S.T. Picraux, J.K. Watanabe, J.W. Mayer, J. Appl. Phys. 79 (1996) 637.
[70] N.V. Nguyen, K. Vedam, J. Appl. Phys. 67 (1990) 3555.
[71] P.A. Aleksandrov, E.K. Baranova, V.V. Budaragin, K.D. Demakov, E.V. Kotov, S.G. Shemardov, Sov. Technic. Phys. Lett. 16 (1990) 902.
[72] K.J. Reeson, P.L.F. Hemment, C.D. Meekison, G.R. Booker, J.A. Kilner, J. Chater, J.R. Davis, G.K. Celler, Appl. Phys. Lett. 50 (1987) 1882.
[73] G.A. Kachurin, I.E. Tyschenko, V.P. Popov, S.A. Tiis, A.E. Plotnikov, Sov. Phys. Semicond. 23 (1989) 271.
[74] M. Deguchi, M. Kitabatake, T. Hirao, N. Arai, T. Izumi, Jpn. J. Appl. Phys. 31 (1992) 343.
[75] I.H. Wilson, in: P. Mazoldi, G. Arnold (Eds.), Ion Beam Modification of Insulators, Elsevier, Amsterdam, 1987, p. 245.
[76] A. Markwitz, H. Baumann, W. Grill, A. Knop, E.F. Krimmel, K. Bethge, Nucl. Instrum. Methods Phys. Res. B 89 (1994) 362.
[77] A. Markwitz, H. Baumann, B. Heinz, A. Roseler, E.F. Krimmel, K. Bethge, J. Fresenius, J. Anal. Chem. 353 (1995) 734.
[78] K.K. Nussupov, N.B. Bejsemkhanov, J. Tokbakov, Nucl. Instrum. Methods Phys. Res. B 103 (1995) 161.
[79] G.F. Cerefolini, L. Meda, Physical Chemistry of, in and on Silicon, Springer Series in Materials Science, vol. 8, Springer, Berlin, 1989.
[80] V. Antonova, G.A. Kachurin, I.E. Tyschenko, S. Shaimeev, Semiconductors 30 (1996) 1051.